POLYMORPH AND POLYTYPE IDENTIFICATION FROM INDIVIDUAL MICA PARTICLES USING SELECTED AREA ELECTRON DIFFRACTION

Anne-Claire Gaillot, Victor A Drits, Bruno Lanson

Clays and Clay Minerals

Polymorph and polytype identification from individual mica particles using selected area electron diffraction

--Manuscript Draft--

Manuscript Number:	CLAY-D-19-00194R2
Full Title:	Polymorph and polytype identification from individual mica particles using selected area electron diffraction
Article Type:	Original Paper
Funding Information:	
Abstract:	Dioctahedral micas are composed of two tetrahedral sheets and one octahedral sheet to form TOT or 2:1 layers. These minerals are widespread and occur with structures differing by (i) the layer stacking mode (polytypes), (ii) the location of vacancies among non-equivalent octahedral sites (polymorphs), and (iii) the charge-compensating interlayer cation and isomorphic substitutions. The potential of parallel-illumination electron diffraction (ED) is assessed here to determine the polytype/polymorph of individual crystals of finely divided dioctahedral micas and to image their morphology. ED patterns are calculated along several zone axes close to the c *- and c -axes using the kinematical approximation for trans - and cis -vacant varieties of the four common mica polytypes (1 M , 2 M 1 , 2 M 2 , and 3 T). When properly oriented, all ED patterns have similar geometry, but differ by their intensity distribution over hk reflections of the zero-order Laue zone. Differences are enhanced for ED patterns calculated along the [001] zone-axis. Identification criteria are proposed for polytype/polymorph identification, based on the qualitative distribution of bright and weak reflections. A database of ED patterns calculated along other zone-axes is provided in case the optimum [001] orientation cannot be found. Different polytype/polymorphs may exhibit similar ED patterns depending on the zone axis considered.
Corresponding Author:	Anne-Claire Gaillot Institut des materiaux Jean Rouxel FRANCE
Corresponding Author Secondary Information:	
Corresponding Author's Institution:	Institut des materiaux Jean Rouxel
Corresponding Author's Secondary Institution:	
First Author:	Anne-Claire Gaillot
First Author Secondary Information:	
Order of Authors:	Anne-Claire Gaillot
	Victor A. Drits
	Bruno Lanson
Order of Authors Secondary Information:	
Author Comments:	Dear Editor, Acting as the corresponding author, I have uploaded the revised version of the manuscript after considering the corrections suggested by the Associate Editor, and moving both figures of the supplementary materials in the main body of the manuscript as suggested. The figures were now provided in the EPS format. Hoping that this version of the manuscript is now suitable for publication, I thank you in advance for your editorialship. Sincerely yours, Anne-Claire GAILLOT

Response to Reviewers:	All corrections suggested by the Associate Editor were implemented in the manuscript, and Figures S1 and S2 initially presented as supplementary materials, were inserted in the main body of the manuscript (now Figures 1 and 3), as suggested by the Associate Editor. Other figures were then renumbered.
Suggested Reviewers:	Buseck Peter pbuseck@asu.edu specialist of TEM and clay structure
	Kenneth Livi klivi@jhu.edu specialist of TEM and clay structure

Polymorph and polytype identification from individual mica particles using selected area electron diffraction

Anne-Claire Gaillot[1,*], Victor A. Drits[2], Bruno Lanson[3]

[1] Université de Nantes, CNRS, Institut des Matériaux Jean Rouxel, IMN, F-44000 Nantes, France

[2] Geological Institute, Russian Academy of Sciences, 7 Pyzhevsky street, 109017 Moscow, Russia

[3] Univ. Grenoble Alpes, CNRS, Univ. Savoie Mont Blanc, IRD, IFSTTAR, ISTerre, F-38000 Grenoble, France

* Author to whom correspondence should be addressed.

e-mail: Anne-Claire.Gaillot@cnrs-imn.fr

Abstract. Dioctahedral micas are composed of two tetrahedral sheets and one octahedral sheet to form TOT or 2:1 layers. These minerals are widespread and occur with structures differing by (i) the layer stacking mode (polytypes), (ii) the location of vacancies among non-equivalent octahedral sites (polymorphs), and (iii) the charge-compensating interlayer cation and isomorphic substitutions. The potential of parallel-illumination electron diffraction (ED) is assessed here to determine the polytype/polymorph of individual crystals of finely divided dioctahedral micas and to image their morphology. ED patterns are calculated along several zone axes close to the **c***- and **c**-axes using the kinematical approximation for *trans*- and *cis*-vacant varieties of the four common mica polytypes (1*M*, 2M_1, 2M_2, and 3*T*). When properly oriented, all ED patterns have similar geometry, but differ by their intensity distribution over *hk* reflections of the zero-order Laue zone. Differences are enhanced for ED patterns calculated along the [001] zone-axis. Identification criteria are proposed for polytype/polymorph identification, based on the qualitative distribution of bright and weak reflections. A database of ED patterns calculated along other zone-axes is provided in case the optimum [001] orientation cannot be found. Different polytype/polymorphs may exhibit similar ED patterns depending on the zone axis considered.

Keywords. Cis-vacant, Dioctahedral mica, Electron diffraction, Illite, Muscovite, Polymorph, Polytype, Trans-vacant, Zone-axis orientation.

INTRODUCTION

K-bearing, aluminous, dioctahedral micas such as illite, muscovite, or phengite, are most abundant in nature and occur, for example, in diagenetically altered sediments, soils, low-grade metamorphic rocks, and igneous and hydrothermal systems (Bailey 1984; Mottana et al. 2004 and references therein). Ideally, their 2:1 layers are composed of a sheet of edge-sharing Al^{3+} octahedra set between two sheets of Si^{4+} tetrahedra. In dioctahedral micas, one out of three octahedral sites is vacant. Isomorphic substitutions can occur both in octahedral and tetrahedral sheets to produce a layer charge deficit which is compensated by interlayer K^{+} cations. Interactions between adjacent layers are relatively weak and produce energetic similarity of polytypes with different layer stacking. Two or more polytypes can coexist even within a crystal. Whereas polytypes differ mainly by their stacking sequences, polymorphs result from different locations of the octahedral vacancy within the 2:1 layer. The average polytypic/polymorphic components of a sample can be determined using X-ray diffraction or thermo-gravimetric analysis (Drits et al. 1984, 1993, 1998; Bailey 1988; Emmerich et al., 1999; Drits & Sakharov 2004; Zviagina et al. 2007). Determining the structure of individual particles requires a local probe and electron microscopy techniques are ideal candidates. Periodicity normal to 2:1 layers and occurrence and nature of stacking faults can be determined from electron diffraction (ED) patterns or high-resolution images collected with the incident electron beam parallel to the layers (Kogure & Banfield 1998; Kogure & Nespolo 1999; Kameda et al. 2007; Kogure & Kameda 2008; Kogure et al. 2008). As a possible alternative to the latter approach, Gaillot et al. (2011) showed that ED patterns collected along the [001] zone axis can also be used to determine the periodicity along the stacking direction from *hk*0 intensities and to obtain structural information such as location of the octahedral vacancy. This method is more limited than when crystals are oriented normal to [001]. A minimal sample preparation (a drop of

a diluted suspension dried on the support) produces many well-oriented crystals quickly and both morphological and structural information is then available.

Morphology of illite, muscovite, or phengite and possibly their (qualitative) chemistry, were shown to be correlated to crystal structure (Lanson et al. 1996, 2002; Patrier et al. 2003; Laverret et al. 2006). This link could not be unambiguously established using global methods such as X-ray diffraction (XRD), thermogravimetric analysis (TGA), or infrared (IR) spectroscopy, however, and the method proposed here thus provides a unique opportunity to (in)validate the established qualitative relationship from the characterization of individual finely divided crystals. If valid, this relationship may be important in determining structure characteristics of mica crystals coating quartz grains in relation to their impact on oil reservoir quality, especially on permeability (Morris & Shepperd 1982; Pallatt et al. 1984; Kantorowicz 1990; Pevear 1999; Wilson et al. 2014). Crystal morphologies ranging from one-dimensional (1D) "hairy" illite to more isometric pseudo-hexagonal 2D plates were reported for illite as a function of maximum burial depth and size fraction in sandstone reservoirs (Lanson et al. 2002 and references therein; Wilson et al. 2014). A structural control on crystal morphology could determine the origin of the morphological variability. The possibility of determining the morphology, dimensions, and crystal structure of individual plates may have implications for crystal growth mechanisms of the different polytype/polymorphs.

Convergent-beam electron diffraction (CBED) patterns can also be used to determine periodicity along the **c***-axis from both *hk*0 and *hk*1 reflections of the zero- and first-order Laue zones (ZOLZ and FOLZ) using minimal sample preparation and crystal orientation (Beermann & Brockamp 2005). CBED application to clay minerals has been limited. First, diffraction intensity is very weak beyond *hk*0 spots and *hk*1 spots from the FOLZ because clay-size micas occur as thin crystals composed mainly of weakly scattering atoms (Si, Al, Mg, O). Second, stacking defects are common even in well-ordered dioctahedral aluminous micas, and the defects induce elongated

reciprocal rods along the **c***-axis. Finally, CBED patterns allows collection of diffraction patterns from a limited crystal surface area (a few nm^2), thus limiting variation in crystal orientation. However, the high electron dose required for CBED pattern collection, with the electron beam fully condensed on mica crystals, often results in sample damage, ranging from amorphization to crystal "drilling". Beam damage also occurs when *cis*-vacant (see below) layers of illite and smectite and *trans*-vacant layers of nontronite are imaged at high resolution. In these cases, layers dehydroxylate owing to the high electron dose which results in cation migration from one octahedral site to another (Kogure & Drits 2010). In contrast, conventional parallel-illumination ED (selected-area electron diffraction, SAED) requires very low electron dose compared to CBED, while producing averaged intensities over a larger ZOLZ area (Vincent & Midgley 1994). SAED allows retrieving layer stacking information in the direction parallel to the electron beam (Gaillot et al. 2011). Information on the vacancy location (polymorphism – *cis*- or *trans*-vacant configuration) can also be obtained for the 1*M* polytype.

Charge-coupled devices (CCD) cameras on microscopes allow recording quantitative intensities for ED spots. Structure identification remains challenging, however, owing to the camera dynamics needed to record ED patterns equal to the high quality achievable with films or recording plates. A small beam stop commonly used to avoid saturating the CCD camera is essential also to avoid masking part of the ED pattern. A small beam stop allows the optimization of orientation during data collection and the analysis of the diffraction intensity distribution. However, intrinsic properties of mica crystals further impair quantitative analysis. The coexistence and interstratification of polytypic and polymorphic varieties within a crystal was addressed by Gaillot et al. (2011), together with the impact of variable crystal thickness on mica ED patterns. In addition, mica plates may be bent, or have growth steps, or variable chemical compositions, which result in inhomogeneous local diffraction conditions. The influence of these additional parameters

on the intensity diffracted by dioctahedral 2:1 micas is investigated in the present study. Identification criteria of mica polytypes are proposed using qualitative intensity distributions within [001] ED patterns, together with a database of ED patterns for a selected set of crystal orientations.

STRUCTURE MODELS AND METHODS

Structure models

The structural formula for K-bearing aluminous dioctahedral micas (Bailey 1984) is:

$$K^{+}_{x+y}{}^{[VI]}(Al^{3+}_{2-y}R^{2+}_{y})\ {}^{[IV]}(Si^{4+}_{4-x}Al^{3+}_{x})O_{10}(OH)_2,\ 0.9 \le x + y \le 1 \qquad (1)$$

where octahedral R^{2+} cations are Mg^{2+} and Fe^{2+}. To simplify structure models, the interlayer site was assumed to host 1.0 K^+ cation per $O_{10}(OH)_2$. Al^{3+}-for-Si^{4+}, and Mg^{2+}-for- Al^{3+} substitutions and H were ignored because they have negligible effects on the structure factors of *hkℓ* reflections, leading to the following simplified composition:

$$K\ {}^{[VI]}Al_2\ {}^{[IV]}Si_4O_{12}\ \text{(to show idealized occupancy).} \qquad (2)$$

A complete $Fe^{2+,3+}$-for-Al^{3+} substitution in the octahedra, as in celadonite [ideally $K\ {}^{[VI]}(Fe^{3+}Fe^{2+})\ {}^{[IV]}Si_4O_{10}(OH)_2$], was investigated to show the effect of the greater scattering. Unit-cell parameters and atomic coordinates were kept constant despite the ionic radii difference between Fe and Al. Similarly, Na^+-for-K^+ replacement, as in paragonite [ideally $Na\ {}^{[VI]}(Al_2)\ {}^{[IV]}(Si_3Al)O_{10}(OH)_2$], on ED intensity distribution was assessed.

Trans- and cis-vacant 1M polymorphs. In ideal one-layer monoclinic (1*M*) mica polytypes, all 2:1 layers have the same azimuthal orientation and the layer displacement T_x is about –*a*/3 along the **a**-axis, **a** being defined from the orthogonal *C*-centered cell described by Bailey

(1988) and given in Table 1 ($b = a\sqrt{3}$, $\gamma = 90°$). Where the octahedral M1 site is empty and M2 and M2' are filled, the 2:1 layer is *trans*-vacant (tv) with a *C*2/*m* symmetry. When the M2 (or M2') site is vacant and M1 and M2' (or M2) sites are occupied, the 2:1 layer is *cis*-vacant (cv) with a *C*2 symmetry (Bailey 1984). The two polymorphs possess identical layer plane unit-cell dimensions (a, b, γ) and layer-to-layer distance ($T_z = c.\sin\beta$) for identical compositions (Drits et al. 1984). They differ however by their layer displacement along the **a**-axis with $T_x = c.\cos\beta$ values of -0.383a and -0.308a, for tv- and cv-1*M*, respectively (Table 1; Drits et al. 1984). Coordinates of the octahedral sites also differ slightly between the two polymorphs. Because tv and cv layers can coexist within 1*M* mica crystals (McCarty & Reynolds 1995; Drits & McCarty 1996; Ylagan et al. 2000), random interstratifications are averaged by diffraction to produce a simplified cell (M-cell). In the average M-cell, the octahedral sheet is not distorted, octahedral sites are partially occupied, and the interlayer displacement T_x is -0.333a (Drits et al. 1984). Crystals with interstratifications having contrasting proportions of tv and cv layers may be described by varying the occupancy of M1, M2, and M2' sites (w_1, w_2, and $w_{2'}$, respectively). For example, $w_1 = 0$ and $w_2 = w_{2'} = 1$ [M-cell with (0:1:1)] correspond to tv-1*M* micas, whereas $w_1 = w_2 = 0.5$ and $w_{2'} = 1$ [M-cell with (0.5:0.5:1)] correspond to the interstratification of tv and cv layers in a 1:1 ratio.

$2M_1$, $2M_2$, and 3T polytypes. In two-layer monoclinic polytypes, successive layers are alternately rotated by ±120° or ±60° ($2M_1$ and $2M_2$ polytypes, respectively). Each **c**-axis forms an oblique angle β with [100] and their projection on the **a**-axis corresponds to the overall layer displacement of ~-a/3 (for 2 layers). In contrast to all other mica polytypes, the **a** vector of the $2M_2$ polytype corresponds to the long dimension of the orthogonal cell in the **ab**-plane (with $a \sim b\sqrt{3}$), thus producing major differences for the orientation of ED patterns and subsequent analysis (see below). In the three-layer trigonal 3*T* polytype, successive layers are rotated by 120° with respect to the preceding layer and the overall layer displacement is null. Structure models of $2M_1$ and 3*T*

polytypes were refined from muscovite and phengite X-ray and neutron diffraction data (#86622 and #75952 of the ICSD database – Amisano-Canesi et al. 1994; Liang et al. 1998), whereas the $2M_2$ model corresponds to the refinement of oblique texture ED data from a natural mica (Zhoukhlistov et al. 1974). Layer chemistry was simplified for each model to match Eq. 2. Cv structures were modeled from those of tv polymorphs by changing occupancy of octahedral sites, while unit-cell parameters and atomic positions were kept unchanged. Unit-cell parameters are listed in Table 1 for all polytypes considered.

Theoretical ED calculations

Dynamical effects are minor for most fined-grained mica crystals of thickness 10-25 nm if the structure consists essentially of light elements (Gaillot et al. 2011). In addition, natural micas occur as mosaic crystals, thus reducing the likelihood of multiple scattering and further minimizing dynamical effects on ED patterns (Drits 1987; Gaillot et al. 2011). To assess this assumption, SAED patterns were collected using 1° and 2° precession angles of the incident electron beam to minimize dynamical diffraction effects (Vincent & Midgley 1994), and compared with ED patterns obtained with no beam precession (Fig. 1). The similarity of ED patterns confirms the quasi absence of dynamical diffraction effects. Consequently, qualitative interpretation of the ED patterns used the kinematical approximation (single scattering event) only with the JEMS simulation software package (Stadelmann, 1999). See Gaillot et al. (2011) for simulation parameters. Intensities are proportional to the square of the structure factor (F^2), modulated by the excitation error *s*. A *s* value of 0.2 nm^{-1} allows matching the extension of the experimental ZOLZ region while excluding contribution from the FOLZ. Calculated intensities are displayed with a spot radius proportional to *F* to mimic intensity differences. Crystal thickness was not considered.

Experimental ED patterns

Origin and chemical compositions of the two illite specimens investigated are described by Gaillot et al. (2011). Briefly, the sample from the Athabasca basin, Canada, contains both tv- and cv-1*M* crystals, whereas the sample from Kombolgie, Australia, is essentially a $2M_1$ illite. Samples were ultrasonically dispersed in de-ionized water and deposited on Cu-mesh grids coated with a holey carbon membrane. SAED patterns were collected on Kodak negative films (Eastman Kodak company, Rochester NY, USA) or with a GATAN CCD camera (Gatan, Pleasanton CA, USA) using a Hitachi H9000 NAR transmission electron microscope (TEM, Hitachi, Okinawa, Japan) equipped with a LaB_6 source and operated at 300 kV and a JEOL *2000fx* LaB_6 TEM operated at 200kV (Jeol, Tokyo, Japan). Complementary Precession ED patterns were acquired on the Nant'Themis, a S/TEM Themis Z G3 (Thermo Fisher Scientific, Whaltman MA, USA) Cs-probe corrected, monochromated, operated at 300 kV and equipped with a Complementary Metal Oxide Semiconductor (CMOS) GATAN OneView camera and the 'Digistar' precession system from NanoMEGAS SPRL (Bruxelles, Belgium).

RESULTS AND DISCUSSION

Finely dispersed mica crystals tend to settle on basal surfaces and lay on grids with the *c**-direction quasi parallel to the electron beam. Intensity distributions of various polytypes oriented along the **c***-axis are not sufficiently contrasting to allow for polytype/polymorph identification, however (see below). Contrast is enhanced when microcrystals are oriented with their [001], i.e., **c**-axis, parallel to the electron beam (Gaillot et al. 2011). Qualitative criteria based on the intensity distribution over *hk*0 spots that are used for identification of the different mica polymorphs and polytypes from their [001] ED patterns are given below.

ED along [001]: geometry, symmetry and indexing

Geometry of [001] ED patterns is similar and all models have the same pseudo-hexagonal arrangement of *hk*0 reflections. Departure from hexagonal symmetry is marginal for 1*M*, $2M_1$, and $2M_2$ polytypes. For 1*M* and $2M_1$ polytypes, indexing was performed with an orthogonal **a*b*** unit cell with a *C*-centered lattice. For the $2M_2$ polytype ($a^* < b^*$), *h*'*k*' indices are obtained from from *h*'*k*' indices of the $2M_1$ by *h*' = *k* and *k*' = -*h*. The orthogonal cell was used for the 3*T* polytype despite its hexagonal symmetry. All ED patterns present mirror planes perpendicular to **a***- and **b***-axes, and *hk*0, $\bar{h}k0$, $h\bar{k}0$, and $\bar{h}\bar{k}0$ reflections are equivalent and are hereafter referred to as *hk* reflections. Intensity distributions for *hk* reflections differ significantly for each polytype (Gaillot et al. 2011).

ED patterns calculated along [001] for 1M polymorphs

Pure tv- and cv-1M polymorphs. ED patterns calculated along [001] for pure tv- and cv-1*M* micas were described by Gaillot et al. (2011). The intensity distribution depends on the layer structure and the occupancy of M1 and M2 sites. For both polymorphs, 06 and 20 spots are strong and 13 and 26 reflections have similar intermediate intensities. The main difference is the intensity of 02 spots, which are much stronger than the 11 reflections for tv-1*M* (Figs. 2a,f), whereas the opposite is observed for cv-1*M* layers (M2 or M2' site vacant, Figs. 2b,g). Similar intensity distributions are obtained when considering M-layers and site occupancies matching those of pure tv- and cv-layers [(0:1:1) and (1:0:1) occupancy probabilities, respectively, Figs. 3a,b].

Partial occupation of octahedral sites. Diffraction patterns for 1*M* crystals in which octahedral vacancies are distributed with equal probability over the two symmetrically related *cis* sites [M-cell with (1:0.5:0.5), Fig. 3c] are similar to that obtained where all vacancies occur in a unique *cis* site (Fig. 2b), except for a limited weakening of 11 reflections and thus a lower contrast with 02 reflections. Similar differences are observed for X-ray diffraction intensity distributions calculated for tv and cv polymorphs (See for example Drits et al. 1984, 1993; Drits & McCarty

1996). Where tv and cv layers coexist with equal probability [M-cell (0.5:0.5:1), Fig. 2k], the resulting ED pattern resembles that calculated for a pure tv layer (Fig. 2a). For a pure tv layer, weaker 02 reflections occur, and a lower intensity contrast exists between 02 and 11 reflections. Intensities of 11 and 02 reflections are identical for tv and cv layers occurring in a 1:2 ratio within crystals. For a 1:2 tv:cv ratio, the intensity of 22 and 04 reflections are increased when vacancies occur equally over the three octahedral sites [M-cell (0.67:0.67:0.67), Fig. 2l] compared to an asymmetric distribution of vacancies over the two *cis* sites [M-cell (0.67:0.33:1), Fig. 3d].

Identification criteria. When oriented along the [001] zone axis, strong 20 and 06 reflections define a diamond-shaped distribution for 1*M* mica polymorphs (dashed line in Figs. 2f,g). In addition, two bright segments parallel to the **a***-axis are defined by 26/06/$\bar{2}$6 and 2$\bar{6}$/0$\bar{6}$/$\bar{2}\bar{6}$ reflections. The ED pattern of the tv-1*M* polymorph is further characterized by a bright diamond defined by 20 and 02 reflections and by two smaller and weaker diamonds defined by 02/13/04/1$\bar{3}$ and 0$\bar{2}$/1$\bar{3}$/04/$\bar{1}\bar{3}$ reflections. In contrast, the ED pattern of the cv-1*M* polymorph exhibits two segments of strong reflections parallel to the **b***-axis and formed by 13/11/1$\bar{1}$/1$\bar{3}$ and $\bar{1}$3/$\bar{1}$1/$\bar{1}\bar{1}$/$\bar{1}\bar{3}$. The intensity distribution of 02 and 11 reflections allows differentiating unambiguously pure tv-, with strong 02 reflections, from pure cv-1*M* polymorphs, with strong 11 reflections. The 11 and 02 reflections are of equal intensity when the M1 and M2 sites are occupied with a ~1:2 ratio (Figs. 2l and 3d). Quantification of *trans vs*. *cis* site occupancy from experimental data remains challenging however owing to the multiple factors influencing ED intensity distribution (see below).

ED patterns calculated along [001] and identification criteria for other tv/cv polytypes

$2M_1$ polymorphs. The [001] ED pattern of tv-$2M_1$ polytype (Fig. 2c) contains three sets of intense *hk* reflections (06 > 20 ≈ 40 > 11 ≈ 26). In contrast to 1*M* polymorphs, the strongest reflections have the same indices for both tv- and cv-$2M_1$ (Fig. 2m). The 22 and 11 reflections are

slightly more intense for the cv-2M_1 polymorph compared to tv-2M_1. However, the small difference in intensity makes the experimental differentiation of the two polymorphs difficult. ED patterns of the 2M_1 exhibits two segments of high-intensity reflections parallel to **a***-axis (defined by 26/06/$\bar{2}$6 and 2$\bar{6}$/0$\bar{6}$/$\bar{2}\bar{6}$ reflections) similar to 1*M* varieties. In addition, a third segment of high-intensity reflections parallel to the **a***-axis is visible (defined by 40 and 20 reflections) together with two triangles of relatively bright reflections (11/1$\bar{1}$/20 and $\bar{1}$1/$\bar{1}\bar{1}$/0$\bar{2}$). For tv-2M_1 polymorphs, these two triangles include 22/2$\bar{2}$ and $\bar{2}$2/$\bar{2}\bar{2}$ reflections, thus resulting in two enlarged and truncated triangles (grey dotted lines in Fig. 2h).

2M_2 polymorphs. For the 2M_2 polytype, the **c**-axis forms an oblique angle with [100], which corresponds to the long **a**-axis by convention, contrary to all other mica polytypes. To reach the [001] zone axis, mica crystals are tilted around the [010] axis which is parallel to the long reciprocal unit-cell vector $\mathbf{v_1}$*. The [001] ED pattern of tv-2M_2 polytype (Fig. 2d) contains three sets of intense reflections: 31 > 11 ≈ 04 reflections. In addition, the 60 spots are weak, whereas 22, 40, and 13 reflections have intermediate intensity, and all other non-extinct *hk* reflections, including 20 spots, are faint. The ED patterns of the 2M_2 differ from all other mica polytypes by the low intensity of 60 reflections compared to other *h*'*k*' reflections and by the absence of bright spots aligned parallel to the **b***-axis. Rather, the 2M_2 is characterized by a large diamond shape defined by 40 and 04 reflections that includes all reflections with non-negligible intensity (dashed line in Fig. 2i). Differentiation of cv and tv with SAED is difficult although 31 reflections dominate the ED pattern for the tv-2M_2 polymorph. These reflections define, together with weaker 11 reflections, two segments of bright spots parallel to the **a***-axis. For the cv-2M_2 polytype, the intensity of the latter reflections is increased making these segments more visible (Fig. 2n). The intensity of 22 reflections is also increased slightly for the cv polymorph compared to the tv polymorph. When vacancies are distributed with equal probability over the two *cis* sites [M-cell (1:0.5:0.5)], 20

reflections appear slightly more intense than 11 spots whereas other reflections are essentially unaffected (not shown).

3T polymorphs. In contrast to previous cases, the [001] direction is parallel to both **c**- and **c***-axes, and the ED pattern for tv-3*T* polytype (Fig. 2e) is hexagonal and exhibits six-fold rotational symmetry, with very strong and of equal intensity 06 and 33 reflections, whereas 11, 02, 22, 04, 26, and 40 spots are weak (Fig. 2j). Vacancy location has a minor influence on the intensity distribution over the ED pattern: 02 and 11 reflections are slightly more intense for the tv-3*T* polymorph whereas 04, 22, 40, and 26 reflections are more intense for the cv-3*T* polymorph (Fig. 2o). These differences are not sufficient to allow experimental differentiation of tv-3*T* and cv-3*T* polymorphs.

Validity of identification criteria

Precession ED criteria. Precession ED (PED) is increasingly used for structure identification or refinement owing to the minimal influence of dynamical effects, with limited electron beams being excited simultaneously (Vincent & Midgley 1994; Gjonnes et al. 1998; Gemmi & Nicolopoulos 2007; Nicolopoulos et al. 2007; Moeck & Rouvimov 2010). These authors showed that intensities are proportional to the structure factor amplitude rather than to its squared value as in conventional ED. Although PED intensities are not equal to the present calculations, qualitative distribution of intensity among bright and weak beams are similar, and identification criteria established above for SAED remain valid (Fig. 1).

Qualitative vs. quantitative criteria. Qualitative, rather than quantitative, identification criteria are proposed in the present work (Figs. 2f-j) because of the limited availability of cameras with sensor dynamics to allow the recording of high-quality ED patterns. In addition, qualitative criteria allow a quick assessment of the polytypic form during observation and a real-time decision for data collection strategy. More importantly, and as discussed hereafter, numerous parameters

influence actual ED intensities beside the crystal structure: i) crystal thickness, which is possible to assess in the microscope by using electron-energy loss spectroscopy (EELS) and analyzing the plasmon peak, or by using beforehand shadowing treatment of the sample; ii) chemical composition, with the implicit requirement of systematic energy dispersive X-ray spectroscopy; and iii) nature and number of structural defects (i.e., random or well-defined translational or rotational stacking faults, interstratification of cv- and tv-layers or of polytypic fragments, etc.). Consequently, systematic quantitative processing of diffracted intensities is unrealistic whereas qualitative identification criteria are useful for polytypic and polymorphic varieties of dioctahedral K-bearing aluminous mica, if only few defects are present and if the mica occurs as thin flat crystals. Intensity ratios may be used to determine structure details, such as the relative proportion of cv and tv layers in 1M crystals from the intensity ratio between 02 and 11 reflections (Figs. 2k,l).

Influence of crystal thickness. ED intensities were calculated here with the kinematical approximation, thus neglecting multiple scattering events that may occur for thick crystals as described by Gaillot et al. (2011). In the absence of beam precession capability to minimize multiple scattering effects, crystal thickness can be estimated *in situ* EELS. Alternatively, the low intensity of diffracted beams compared to the direct beam will ensure that crystals are sufficiently thin to interpret intensity distribution among $hk\ell$ spots (h and $k \leq 6$). In any case, reported intensity distributions based on kinematical approximation, are probably sufficient to qualitatively interpret SAED patterns and to identify polytypes and polymorphs for most crystals of microcrystalline micas, containing mostly light elements (Gaillot et al. 2011).

Influence of local unit-cell distortions. Except for the 1*M* polytype, structure models (Zhoukhlistov et al. 1973, 1974; Drits et al. 1984, 2010a, 2010b; Amisano-Canesi et al. 1994; Liang et al. 1998) used for the calculations reported here were systematically refined for tv layer configuration. As noted above, diffraction effects from cv polymorphs and structures where tv and

cv layers coexist were calculated by varying the w_i occupancy of M1, M2, and M2' sites without adjustment of atomic positions. Comparison of ED patterns calculated for tv-1*M* and cv-1*M* models with adjustment of atomic positions and for the average M-layer with equivalent octahedral site occupancies (0:1:1 and 1:0:1, respectively) indicates the sensitivity of ED patterns to local distortions within the unit cell (Figs. 3a,b). This influence remains limited, however, and qualitative identification criteria remain valid for cv polymorphs of 2*M* and 3*T* polytypes. Similarly, local distortions induced by cationic substitutions can be ignored as a first approximation. However, as the occupancy of M2 and M2' sites within cv-1*M* crystals influences the intensity distribution, the coexistence of vacant M2 and M2' sites within cv-1*M* crystals possibly accounts for the experimental absence of expected dynamical effects, such as center of symmetry loss for cv layers (Gaillot et al. 2011).

Influence of crystal bending. Owing to the size of the selected-area aperture, ED intensities are averaged over a large surface area of the crystal (typically ~200 nm in diameter, although a smaller aperture can be used, if available). Variation in surface orientation with respect to the electron beam, often revealed by bending contours in the image, results in diffracted intensities being averaged, similar to mosaicity effects. Moving a small aperture over the crystal allows assessing the effect of bending. For investigated crystals, diffraction mapping at the nanoscale showed that the orientation fluctuation remains <1-2° (not shown). As long as the crystal surface bending is small (<1-2°), a distinctive pattern of a given polytype should be recognizable.

Influence of chemical composition on dioctahedral mica ED patterns

Mg^{2+}-for-Al^{3+} or Al^{3+}-for-Si^{4+} substitutions in octahedral and tetrahedral sheets have marginal influence on diffracted intensity distributions owing to the similar scattering factors of involved cations. Other cation substitutions are frequent in natural dioctahedral micas, the most common being Na^{+}-for-K^{+} in paragonite and the partial substitution of Fe^{2+}/Fe^{3+} for Al^{3+} in illite

and phengite, and in celadonite and glauconite (Bailey 1984; Mottana et al. 2004). The influence of Na^{+}-for-K^{+} and Fe^{2+}/Fe^{3+}-for-Al^{3+} substitutions on ED intensity is described below for the mica polytypes. Expected lattice distortions induced by cationic radii variations or vacant octahedral sites are not considered owing to their limited effect on diffraction intensity.

Na-bearing aluminous dioctahedral mica. Intensity distributions among *hk* reflections calculated for tv-1*M*, cv-1*M*, tv-2M_1, tv-2M_2, and tv-3*T* structure models and an idealized paragonite composition ($Na^{[VI]}Al_2{}^{[IV]}Si_4O_{12}$, Figs. 4a-e) differ slightly from a muscovite composition ($K^{[VI]}Al_2{}^{[IV]}Si_4O_{12}$, Figs. 2a-e). However, 02 and/or 11 reflections are stronger for Na vs. K micas, whereas 06 reflections are weaker. Furthermore, because 02 reflections dominate the tv-1*M* ED pattern, and 11 reflections dominate the cv-1*M* polymorph, the difference between tv-vs. cv-1*M* is enhanced for sodic micas.

K-bearing ferruginous dioctahedral mica. Differences in intensity distributions calculated for tv-1*M*, cv-1*M*, tv-2M_1, tv-2M_2 and tv-3*T* models and either an idealized celadonite composition ($K^{[VI]}Fe_2{}^{[IV]}Si_4O_{12}$, Figs. 4f-j) or a muscovite composition (Figs. 2a-e) are marginal despite the scattering contrast between Fe and Al/Mg. For example, [001] ED patterns are similar for ferruginous and aluminous varieties of tv-3*T* and tv-2M_2 micas. For tv-2M_1 micas, all reflections but 06 and 40 are weaker for the ferruginous variety compared to the aluminous mica, whereas for tv-1*M* and cv-1*M* polymorphs, 13 reflections are weaker and 26 spots stronger for the ferruginous mica compared to the aluminous mica. In all cases, the overall intensity distribution, and the sets of bright *hk* spots are similar for both ferruginous and aluminous varieties.

ED patterns along other crystal orientations

Except for the 3*T* polytype, whose **c**-axis is perpendicular to the layer plane, all mica crystals must be rotated to be oriented along the [001] axis, the direction of which is unknown a

priori. To reach the [001] axis, which forms an oblique angle with [100] (Fig. 5a), crystals that lay on the **ab**-plane must be rotated by a θ_{th} angle around the [010] axis. Two directions of rotation ($\pm\theta$) are possible to reach the [001] zone axis. In practice, the closest zone axis is easily reached, but may differ from the [001] axis. Indeed [001] and [101] axis are tilted at about the same angle (~10°) in opposite directions for 1M polytypes. To more rapidly allow for a correct identification of SAED patterns oriented along [001], additional calculations were performed along a selection of [$hk\ell$] zone axes near the **c**-axis (Fig. 5a). Theoretical θ_{th} angles between the **c***-axis and [$hk\ell$] directions are provided in Figures 6-7, although experimentally determined values may deviate slightly if crystals are not normal to the electron beam.

*ED patterns calculated along the **c***-axis.* The **c***-axis is close to [103] for 1*M*, 2M_1, and 2M_2 polytypes ($\theta_{th} \leq 1.5°$) and perpendicular to the 2:1 layers, thus producing hexagonal ED patterns, similar to the 3*T* polytype along [001]. For all polytypes, *hk* reflections from the third hexagon (06 and 33 reflections) are of equal intensity and dominate the ED pattern (Figs. 6a-e). The ED pattern calculated for the 3*T* polytype is the only ED showing a six-fold axis, whereas those calculated for monoclinic polytypes (1*M*, 2M_1, and 2M_2) exhibit two mirror planes normal to $\mathbf{a}_{//}$***** (projection of **a*** on the ZOLZ plane) and **b*** vectors, *hkl* reflections with $h = 3n$ being the only ones observed. For well-ordered crystals, extinction rules can be used as an identification criterion. Extinction rules may be violated, owing to reciprocal lattice node elongation for defective or very thin crystals.

Tilt around [010]. The geometry and intensity distributions of calculated ED patterns depend on the [*u*0*w*] zone axis considered. As a rule, relative intensities of 0*k*0 spots along the common **b***-axis are preserved. For crystals oriented along the [102] zone axis, the ZOLZ also contains $-2l\ k\ l$ reflections (with the $h + k = -w \times l + k = 2n$ extinction rule from C-centering). *hk* reflections with $h \neq 2l$ do not theoretically appear (unless the reciprocal rods are sufficiently

elongated) leading to rectangular patterns of the brightest spots (Figs. 6f-j). For increasing tilt values (Fig. 5a), the geometry of [101] and [$\bar{1}$01] ED patterns (Figs. 6k-t) remains similar to that of patterns calculated along [001] (Figs. 2a-e) with only a faint stretching along the $a_{//}$***** direction. This elongation becomes significant for ED patterns calculated along [*h*01] with $|h| \geq 2$, although the intensity distribution may be still useful for polytype identification (Figs. 7a-o). ED patterns calculated along other [*h*0ℓ] axes are less informative. ED patterns for tv-2M_1 along [101] and for cv-1*M* along [001] are alike (Figs. 6m and 4b, respectively), as are those for tv-3*T* along [101] and for 1*M* with the vacancies equally distributed over the three octahedral sites (Figs. 6o and 4l). Similarly, ED patterns for tv-2M_1 along [$\bar{1}$01] and for cv-1*M* along [101] are alike (Figs. 6r and 6l), as are those for tv-3*T* along the **c-** or **c***-axis and for tv-1*M*, cv-1*M*, and tv-2M_1 along [103], at least for the intensity distribution among most intense reflections (Figs. 6e and 6a-c, respectively). These similarities may require recording an additional ED pattern along another [10*w*] ZA to determine the [001] axis.

Tilt around [100]. ED patterns calculated along [011] for *t*v-1*M*, *c*v-1*M*, tv-2M_1, tv-2M_2, and tv-3*T* polytypes are shown in Figure 7p-t. For monoclinic polytypes, [001] and [100] form an oblique angle. The angle between **a**$_{//}$***** and **b***-axis thus differs from 90° and ED patterns calculated along [011] appear significantly distorted. In addition, ED patterns calculated along [0*k*1], with $k \neq 0$, possess lower symmetry than those calculated along [001] and the former no longer present mirror planes (even for the 3*T* polytype) because intensities of *hk*ℓ, $h\bar{k}\ell$, and equivalent reflections are no longer equal. The center of symmetry is preserved however with I(*hk*ℓ) = I($\bar{h}\bar{k}\bar{\ell}$) for kinematical diffraction (Friedel's law). Symmetry lowering makes ED patterns recorded along [0*k*1] recognizable.

Advanced identification method

Different polytypes can have similar ED patterns along different zone axes, thus impairing polytype identification if the [001] zone axis is not correctly determined. Although complementary powder X-ray diffraction data indicate the major polytypes present in a sample, a suitable orientation along [001] is key to avoid polytype misidentification using the proposed criteria (Figs. 2f-j). Orientation along [001] relies on the correct identification of the [010] rotation axis and on the inclination θ of the zone axis relative to the **c***-axis. ED patterns along several crystallographic directions can be useful to further constrain polytype/polymorph identification if the crystal orientation is uncertain.

Experimental considerations. In practice, determining the appropriate rotation direction to reach the [001] axis can be challenging. A large number of stacking faults present may negate any effort, however, as the [001] direction is not unique, and thus thin crystals are usually preferred. Crystal morphology is also used to determine ED pattern orientation in the a*-b*-plane because unit-cell **a** or **b** vectors are often parallel to a crystal edge. In addition, illite lath-shaped crystals grow parallel to the [100] (Rex 1964), and the [001] axis can be reached by rotating the crystal around the direction parallel to the short dimension (Figs. 8a-b). There is no absolute method to determine a priori how the rotation should be performed and a trial-and-error approach is necessary. However, the [001] ED patterns must possess two perpendicular mirror planes common to all patterns oriented along [u0w] axes. If this symmetry is fulfilled, experimental SAED pattern can be compared with calculated patterns (Figs. 2 and 6) for identification. Additional tilt in the same or opposite directions allows reaching other [u0w] orientations to confirm polytype identification.

Experimental zone axis angle. Ideally, the **b***-axis is aligned with the sample holder primary rotation axis (the "Tilt" axis) and the tilt angle to reach the desired [u0w] orientation can be compared directly to the theoretical θ_{th} value (indicated in the figures). In practice, this is

achieved with a "Tilt-Rotation" holder that allows rotating the sample within the observation plane. With commonly available "Double Tilt" holders, obtaining the correct orientation requires combining two rotation axes (Tilt and Azimuth angles, Fig. 5b), both normal to the electron beam. In cylindrical coordinates, the inclination of the ED pattern zone axis with respect to the crystal **c***-axis is defined by two angles: θ and Ω, the angles with the ***z***-direction and between the projection of the zone axis on the **ab**-plane and the sample holder primary rotation (tilt) x-axis, respectively. Experimental Ω and θ angles can be computed from sample holder tilt (*Tt*) and azimuth (*Az*) rotation angles using the following equations:

$$\frac{d_y}{d_x} = \tan\Omega = \frac{\tan Tt}{\tan Az}\text{ , }\Omega = 90° \text{ if } Az = 0° \quad (3)$$

$$\frac{d_x{}^2 + d_y{}^2}{h^2} = \tan^2\theta = \tan^2 Az + \tan^2 Tt \quad (4)$$

where d_x, d_y, h are the coordinates (in Å) of a virtual point (M) on the zone axis, along the two rotation axes (x, y) and the electron beam (z) directions, respectively (Fig. 5c). Conversely, it is possible to calculate *Tt* and *Az* values to be used experimentally from the θ and Ω angles of the sought zone axis:

$$\tan Tt = \frac{\tan\theta.\tan\Omega}{\sqrt{1+\tan^2\Omega}} \quad (5)$$

$$\tan Az = \frac{\tan\theta}{\sqrt{1+\tan^2\Omega}} \quad (6)$$

These equations may aid in finding the orientation of the first [*u*0*w*] zone axis from the initial crystal orientation with the **c***-axis close to the beam direction. The equations can also be used for multiple zone-axis data collection. In the latter case, the crystal shift upon tilting must be compensated if the crystal is not flat. To illustrate, SAED patterns were obtained for two

orientations from isomorphic plates of illite from Kombolgie (Figs. 8c-d). For both patterns, the $|\theta_{exp}|$ angle calculated from the TEM holder angles (~12° and 3°, respectively) is consistent with the theoretical $|\theta_{th}|$ value calculated for the [101] and [001] ZA of the $2M_1$ polytype (~9° and 6°, respectively), thus obtaining a determination of the $2M_1$ polytype, despite the minor discrepancy between experimental and calculated tilt angles.

SUMMARY AND PERSPECTIVES

Qualitative criteria are provided to determine the polymorph/polytype of individual crystals of K-bearing aluminous dioctahedral micas from the intensity distribution of *hk* reflections from the zero-order Laue zone. Differences are enhanced for ED patterns calculated along the [001] zone-axis. ED patterns calculated along adjacent zone-axes are provided to avoid potential difficulties in obtaining unambiguously the optimum [001] orientation. The method allows retrieving morphological and structural information from individual mica crystals. Matching the observed data to calculated patterns allows the determination of structural information from K-bearing aluminous mica crystals (illite, muscovite, or phengite), including morphology and possibly chemistry (Lanson et al. 1996, 2002; Patrier et al. 2003; Laverret et al. 2006).

ACKNOWLEDGMENTS

Daniel Beaufort (IC2MP, Poitiers – France) is thanked for providing the $1M$ illite and $2M_1$ muscovite samples. Funded by the French Contrat Plan État-Région and the European Regional Development Fund of Pays de la Loire, the CIMEN Electron Microscopy Center in Nantes is greatly acknowledged. ISTerre is part of Labex OSUG@2020 (ANR10 LABX56). Comments by two anonymous reviewers improved and clarified the initial manuscript. On behalf of all authors, the corresponding author states that there is no conflict of interest.

REFERENCES

Amisano-Canesi, A., Chiari, G., Ferraris, G., Ivaldi, G., & Soboleva, S.V. (1994) Muscovite-3*T* and phengite-3*T* - crystal-structure and conditions of formation. *European Journal of Mineralogy*, *6*, 489-496.

Bailey, S.W. (1984) Classification and structure of the micas. Pp. 1-12. In S.W. Bailey, Ed. *Micas*, 13,Mineralogical Society of America, Chantilly, Va.

Bailey, S.W. (1988) *Hydrous phyllosilicates (exclusive of micas).* Pp. 725. Mineralogical Society of America, Chantilly, Va.

Beermann, T. & Brockamp, O. (2005) Structure and analysis of montmorillonite crystallites by convergent-beam electron diffraction. *Clay Minerals*, *40*, 1-13.

Drits, V.A. (1987) *Electron diffraction and high-resolution electron microscopy of mineral structures*. Pp. 304. Spring-Verlag, New-York.

Drits, V.A. & McCarty, D.K. (1996) The nature of diffraction effects from illite and illite-smectite consisting of interstratified trans-vacant and cis-vacant 2:1 layers: A semiquantitative technique for determination of layer-type content. *American Mineralogist*, *81*, 852-863.

Drits, V.A. & Sakharov, B.A. (2004) Potential problems in the interpretation of powder X-ray diffraction patterns from fine-dispersed 2M_1 and 3*T* dioctahedral micas. *European Journal of Mineralogy*, *16*, 99-110.

Drits, V.A., Plançon, A., Sakharov, B.A., Besson, G., Tsipursky, S.I., & Tchoubar, C. (1984) Diffraction effects calculated for structural models of K-saturated montmorillonite containing different types of defects. *Clay Minerals*, *19*, 541-562.

Drits, V.A., Weber, F., Salyn, A.L., & Tsipursky, S.I. (1993) X-ray identification of one-layer illite varieties: Application to the study of illites around uranium deposits of Canada. *Clays and Clay Minerals*, *41*, 389-398.

Drits, V.A., Lindgreen, H., Salyn, A.L., Ylagan, R.F., & McCarty, D.K. (1998) Semiquantitative determination of *trans*-vacant and *cis*-vacant 2:1 layers in illites and illite-smectites by thermal analysis and X-ray diffraction. *American Mineralogist, 83*, 1188-1198.

Drits, V.A., Ivanovskaya, T.A., Sakharov, B.A., Zvyagina, B.B., Derkowski, A., Gor'kova, N.V., Pokrovskaya, E.V., Savichev, A.T., & Zaitseva, T.S. (2010a) Nature of the structural and crystal-chemical heterogeneity of the Mg-rich glauconite (Riphean, Anabar uplift). *Lithology and Mineral Resources, 45*, 555-576.

Drits, V.A., Zviagina, B.B., McCarty, D.K., & Salyn, A.L. (2010b) Factors responsible for crystal-chemical variations in the solid solutions from illite to aluminoceladonite and from glauconite to celadonite. *American Mineralogist, 95*, 348-361.

Emmerich, K., Madsen, F.T., & Kahr, G. (1999) Dehydroxylation behavior of heat-treated and steam-treated homoionic *cis*-vacant montmorillonites. *Clays and Clay Minerals*, *47*, 591-604.

Gaillot, A.-C., Drits, V.A., Veblen, D.R., & Lanson, B. (2011) Polytype and polymorph identification of finely divided aluminous dioctahedral mica individual crystals with SAED. Kinematical and dynamical electron diffraction. *Physics and Chemistry of Minerals, 38*, 435-448.

Gemmi, M. & Nicolopoulos, S. (2007) Structure solution with three-dimensional sets of precessed electron diffraction intensities. *Ultramicroscopy, 107*, 403-494.

Gjonnes, J., Hansen, V., Berg, B.S., Runde, P., Cheng, Y.E., Gjonnes, K., Dorset, D.L., & Gilmore, C.J. (1998) Structure model for the phase Al_mFe derived from three-dimensional electron diffraction intensity data collected by a precession technique. Comparison with convergent-beam diffraction. *Acta Crystallographica*, *A54*, 306-319.

Kameda, J., Miyawaki, R., Kitagawa, R., & Kogure, T. (2007) XRD and HRTEM analyses of stacking structures in sudoite, di-trioctahedral chlorite. *American Mineralogist*, *92*, 1586–1592.

Kogure, T. & Banfield, J.F. (1998) Direct identification of the six polytypes of chlorite characterized by semi-random stacking. *American Mineralogist*, *83*, 925-930.

Kogure, T. & Drits, V.A. (2010) Structural change in celadonite and *cis*-vacant illite by electron radiation in TEM. *Clays and Clay Minerals*, *58*, 522-531.

Kogure, T. & Kameda, J. (2008) High-resolution TEM and XRD simulation of stacking disorder in 2:1 phyllosilicates. *Zeitschrift für Kristallographie*, *223*, 69-75.

Kogure, T. & Nespolo, M. (1999) First occurrence of a stacking sequence including (+60°, 180°) rotations in Mg-rich annite. *Clays and Clay Minerals*, *47*, 784-792.

Kogure, T., Kameda, J., & Drits, V.A. (2008) Stacking faults with 180° layer rotation in celadonite, an Fe- and Mg-rich dioctahedral mica. *Clays and Clay Minerals*, *56*, 612-621.

Lanson, B., Beaufort, D., Berger, G., Baradat, J., & Lacharpagne, J.-C. (1996) Illitization of diagenetic kaolinite-to-dickite conversion series: Late-stage diagenesis of the lower Permian Rotliegend sandstone reservoir, offshore of The Netherlands. *Journal of Sedimentary Research*, *66*, 501-518.

Lanson, B., Beaufort, D., Berger, G., Bauer, A., Cassagnabere, A., & Meunier, A. (2002) Authigenic kaolin and illitic minerals during burial diagenesis of sandstones: A review. *Clay Minerals*, *37*, 1-22.

Laverret, E., Patrier Mas, P., Beaufort, D., Kister, P., Quirt, D., Bruneton, P., & Clauer, N. (2006) Mineralogy and geochemistry of the host-rock alterations associated with the Shea creek unconformity-type uranium deposits (Athabasca basin, Saskatchewan, Canada). Part 1. Spatial variation of illite properties. *Clays and Clay Minerals*, *54*, 275-294.

Liang, J.J., Hawthorne, F.C., & Swainson, I.P. (1998) Triclinic muscovite: X-ray diffraction, neutron diffraction and photo-acoustic FTIR spectroscopy. *Canadian Mineralogist*, *36*, 1017-1027.

McCarty, D.K. & Reynolds, R.C., Jr. (1995) Rotationally disordered illite/smectite in paleozoic K-bentonites. *Clays and Clay Minerals*, *43*, 271-284.

Moeck, P. & Rouvimov, S. (2010) Precession electron diffraction and its advantages for structural fingerprinting in the transmission electron microscope. *Zeitschift für Kristallographie*, *225*, 110–124.

Mottana, A., Sassi, F.P., Thompson, J.B., Jr, & Guggenheim, S. (2004) *Micas: Crystal chemistry and metamorphic petrology*. Pp. 499. Mineralogical Society of America, Chantilly, Va.

Nicolopoulos, S., Morniroli, J.-P., & Gemmi, M. (2007) From powder diffraction to structure resolution of nanocrystals by precession electron diffraction. *Zeitschift für Kristallographie. Supplement issue 26*, 183-188.

Patrier, P., Beaufort, D., Laverret, E., & Bruneton, P. (2003) High-grade diagenetic dickite and 2M_1 illite from the middle Proterozoic Kombolgie formation (Northern Territory, Australia). *Clays and Clay Minerals*, *51*, 102-116.

554 Rex, R.W. (1964) Authigenic kaolinite and mica as evidence for phase equilibria at low
555 temperature. *Clays and Clay Minerals*, *13*, 95-104.

556 Stadelmann, P. (1999) Electron Microscopy Suite, Java version (JEMS). CIME-EMPL,
557 Switzerland.

558 Vincent, R. & Midgley, P.A. (1994) Double conical beam-rocking system for measurement of
559 integrated electron diffraction intensities. *Ultramicroscopy*, *53*, 271-282.

560 Ylagan, R.F., Altaner, S.P., & Pozzuoli, A. (2000) Reaction mechanisms of smectite illitization
561 associated with hydrothermal alteration from ponza island. *Clays and Clay Minerals*, *48*,
562 610-631.

563 Zhoukhlistov, A.P., Zvyagin, B.B., Soboleva, S.V., & Fedotov, A.F. (1973) The crystal structure
564 of the dioctahedral mica $2M_2$ determined by high voltage electron diffraction. *Clays and*
565 *Clay Minerals*, *21*, 465-470.

566 Zhoukhlistov, A.P., Zvyagin, B.B., Soboleva, S.V., & Fedotov, A.F. (1974) Structure of a
567 dioctahedral mica $2M_2$ according to high-voltage electron diffraction data (in Russian).
568 *Doklady Akademii Nauk SSSR*, *219*, 704-707.

569 Zviagina, B.B., Sakharov, B.A., & Drits, V.A. (2007) X-ray diffraction criteria for the
570 identification of *trans*- and *cis*-vacant varieties of dioctahedral micas. *Clays and Clay*
571 *Minerals*, *55*, 467-480.

572

573 FIGURE CAPTIONS

574 Figure 1. (**a**) Transmission electron micrograph of an isomorphic illite particle from Athabasca
575 Basin. (b-c) Corresponding experimental SAED patterns along [001] acquired on the circled zone
576 and recorded (**b**) without precession, and (**c**) with a 2° angle precession of the electron beam.

577 Figure 2. ED patterns calculated using the kinematical approximation along the [001] zone axis for
578 different polymorphs/polytypes: (**Left, from a-e**) tv-1*M*; cv-1*M*; tv-2M_1; tv-2M_2; tv-3*T*. Numerical
579 values indicate the theoretical θ_{th} angle between the [001] zone axis and the normal to the **ab**-plane
580 of the crystal. (**Middle, from f-j**) Corresponding schematic identification diagrams. Disk diameter
581 and grey-scale intensity correspond to the intensity scale of the main *hk*0 reflections. Solid lines
582 connect most intense *hk*0 reflections. (**Right**) Additional ED calculations: (**k**) 1*M* polytype
583 considering M-cell (0.5:0.5:1); (**l**) 1*M* polytype considering M-cell (0.67:0.67:0.67); (**m**) cv-2M_1
584 polymorph; (**n**) cv-2M_2 polymorph; (**o**) cv-3*T* polymorph.

585 Figure 3. ED patterns calculated using the kinematical approximation along the [001] zone axis for
586 the 1M polytype considering the M-cell, for different occupancies (w1:w2:w2') of the octahedral
587 M1, M2 and M2' sites : (**a**) pure tv model with M1 site empty (0:1:1); (**b**) pure cv model with M2
588 site empty (1:0:1); (**c**) cv model with the M2 and M2' sites equally vacant (1:0.5:0.5); (**d**) model
589 with an asymmetrical distribution of vacancies (0.67:0.33:1) as occurring when tv and cv layers
590 occur in a 1:2 ratio within the crystal. hk indices are given for the brightest spots ($\ell = 0$).

591 Figure 4. ED patterns calculated along the [001] zone axis for different polytypes and polymorphs
592 of (**left**) Na-rich aluminous dioctahedral mica ($NaAl_2Si_4O_{12}$) and (**right**) K-rich ferrous
593 dioctahedral mica ($KFe_2Si_4O_{12}$). (**a-e** and **f-j**) tv-1*M*; cv-1*M*; tv-2M_1; tv-2M_2; tv-3*T*. Unit-cell axes
594 for cv-1*M*, tv-2M_1 and tv-3*T* are identical to tv-1*M*.

595 Figure **5.** (**a**) Orientation of different zone axes with respect to the **a** (or **a'**) = [100] and **c** = [001]
596 axes of the mica unit cell shown in projection along the **b-** (or **b'-**) axis. (**b**) Direction of tilt (Tt)
597 and azimuth (Az) rotation angles for a double-tilt sample holder. (**c**) Decomposition of the θ angle
598 between considered zone axis and the electron beam direction on both *Tt* and *Az* rotation angles of
599 the TEM holder shown in (**b**).

600 Figure 6. ED patterns calculated for various mica polymorphs and polytypes along different zone
601 axes: (**from left to right**) [103] (except for (**e**) [001]); [102]; [101] and [1; $\bar{}$01] ZA. (**top to bottom**)
602 tv-1*M*; cv-1*M*; tv-2M_1; tv-2M_2; tv-3*T*. Unit-cell vectors for cv-1*M*, tv-2M_1 and tv-3*T* are identical
603 to tv-1*M*. Numerical values as in Fig. 1. *hk* indices are indicated above the brightest reflexions,
604 their *l* indices on the side for tv-1M (same for (below for 2M_2).

605 Figure 7. ED patterns calculated for various mica polymorphs and polytypes along different zone
606 axes: (**from left to right**) [201]; [301]; [2; $\bar{}$01] and [011] ZA. (**top to bottom**) tv-1*M*; cv-1*M*; tv-
607 2M_1; tv-2M_2; tv-3*T*. Unit-cell vectors and numerical values as in Figs. 1 and 4.

608 Figure 8. (**a**) Transmission electron micrographs of Athabasca Basin illite isomorphic and lath-
609 shaped crystals; (**b**) Experimental SAED along [001] from the circled zone of the lath crystal with
610 $|\theta|$ ~10°; (**c-d**) Experimental SAED along [101] and [001] respectively of isomorphic Kombolgie
611 illite crystal with experimental Tilt and Azimuthal TEM holder angles, and corresponding ZA
612 inclination $|\theta_{exp}|$ with respect to **c***-axis deduced from Eqs. 3-4.

613 Table 1. Unit-cell parameters for tv-1*M*, cv-1*M*, tv-2$M_1$and tv-3*T* polytypes ($\alpha = \beta = 90°$)

Polytype	a (Å)	b (Å)	c (Å)	γ (°)
tv-1*M*	5.199	9.005	10.164	101.3
cv-1*M*	5.199	9.005	10.090	99.13
M-layer	5.199	9.005	10.12	99.86
tv-2M_1	5.177	8.987	20.072	95.76
tv-2M_2*	9.023	5.197	20.171	99.48
tv-3*T*	5.212	9.027	29.804	90

* Unit-cell parameters listed in the Russian version of the article (Zhoukhlistov *et al.*, 1973) slightly differ from those reported in an earlier English version and found in the ICSD database (#89823)

614

Figure

Click here to access/download;Figure;Figure 1.eps

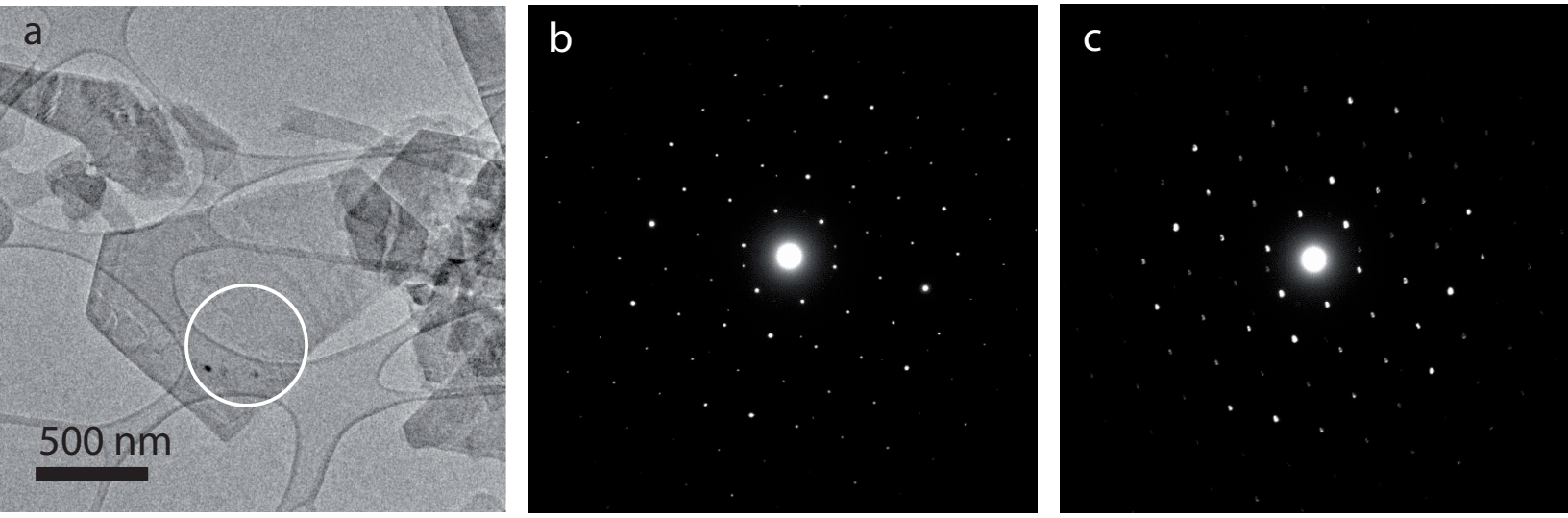

Gaillot et al. - Figure 1

Figure

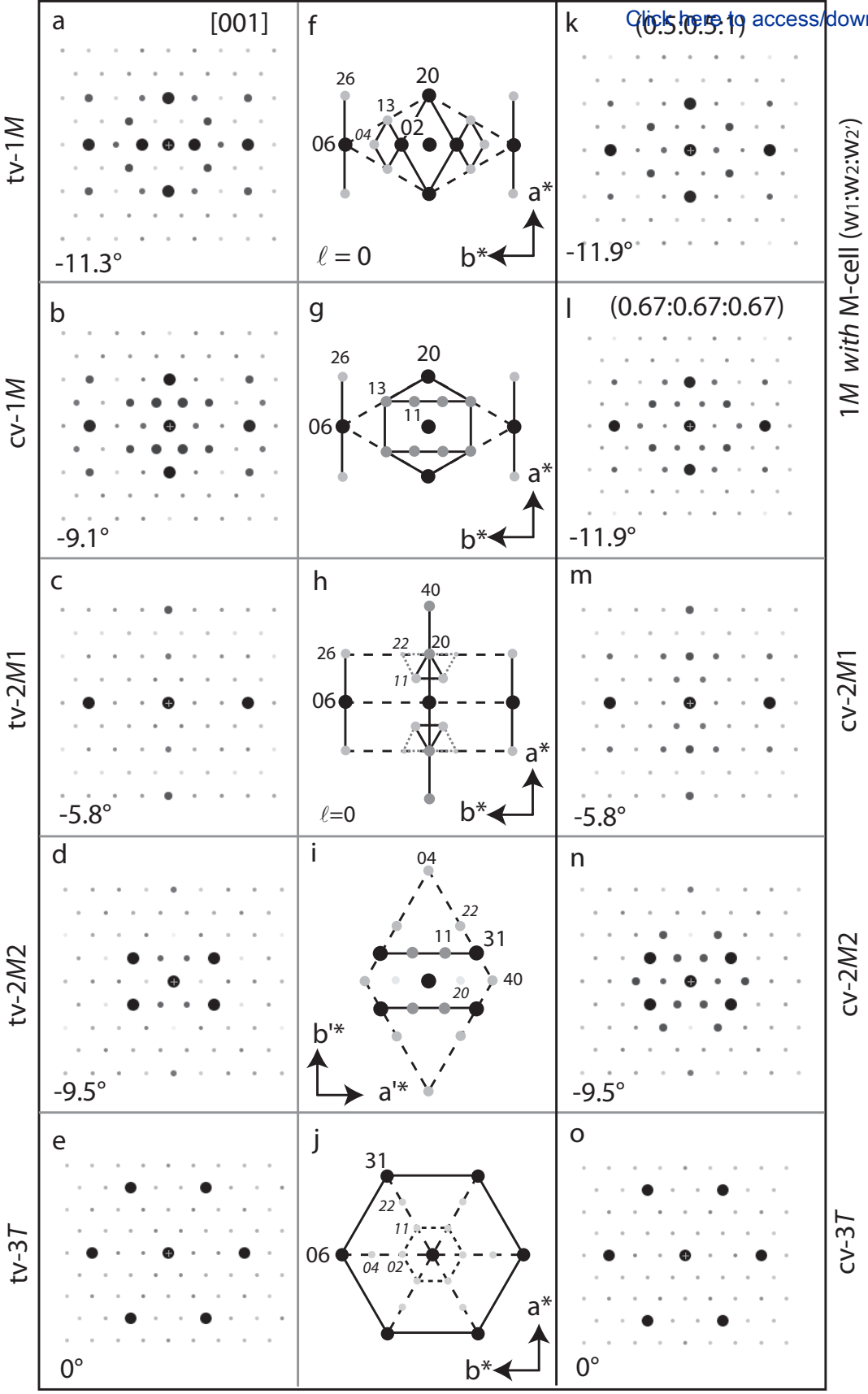

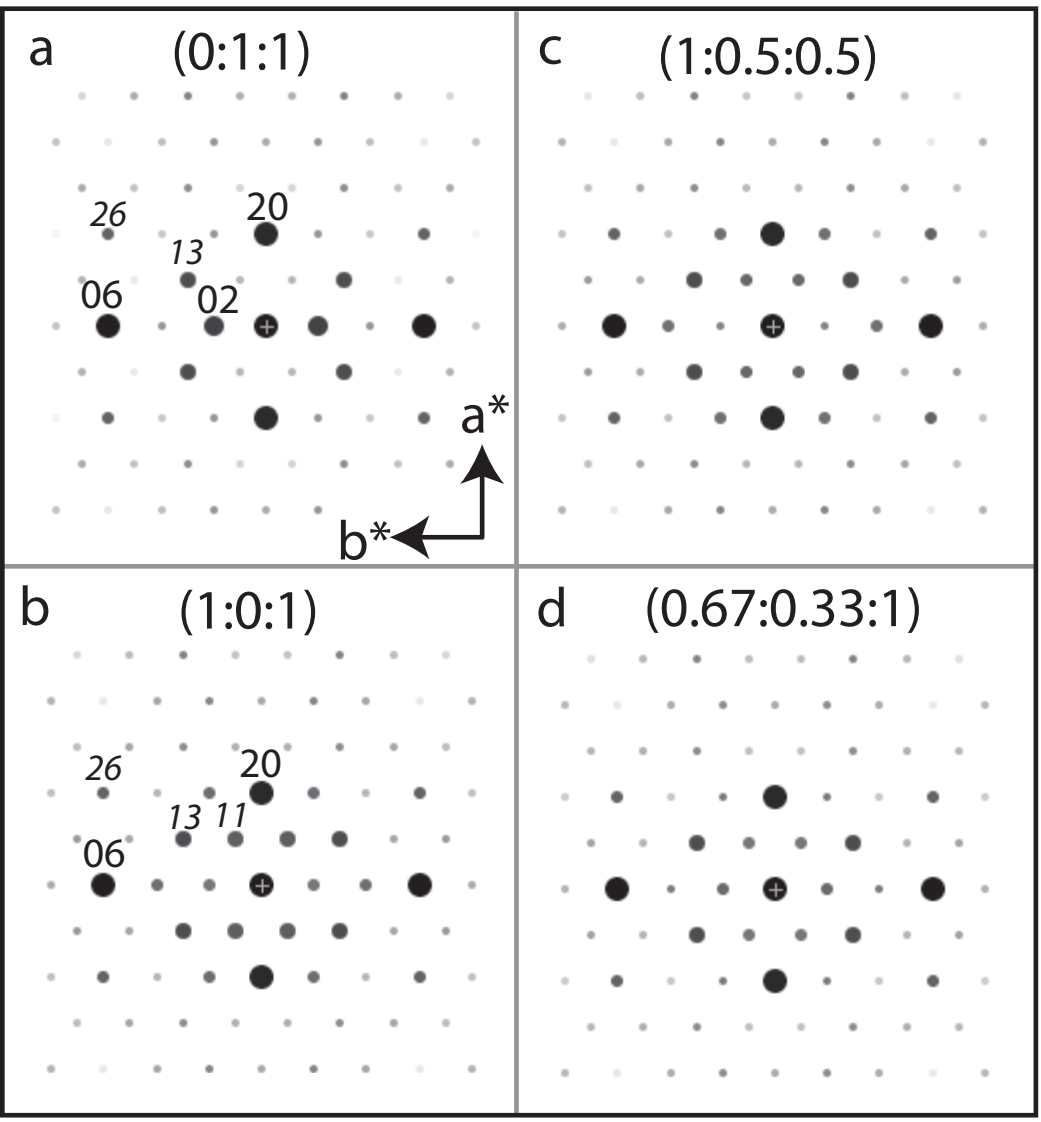

Gaillot et al. - Figure 3

Figure

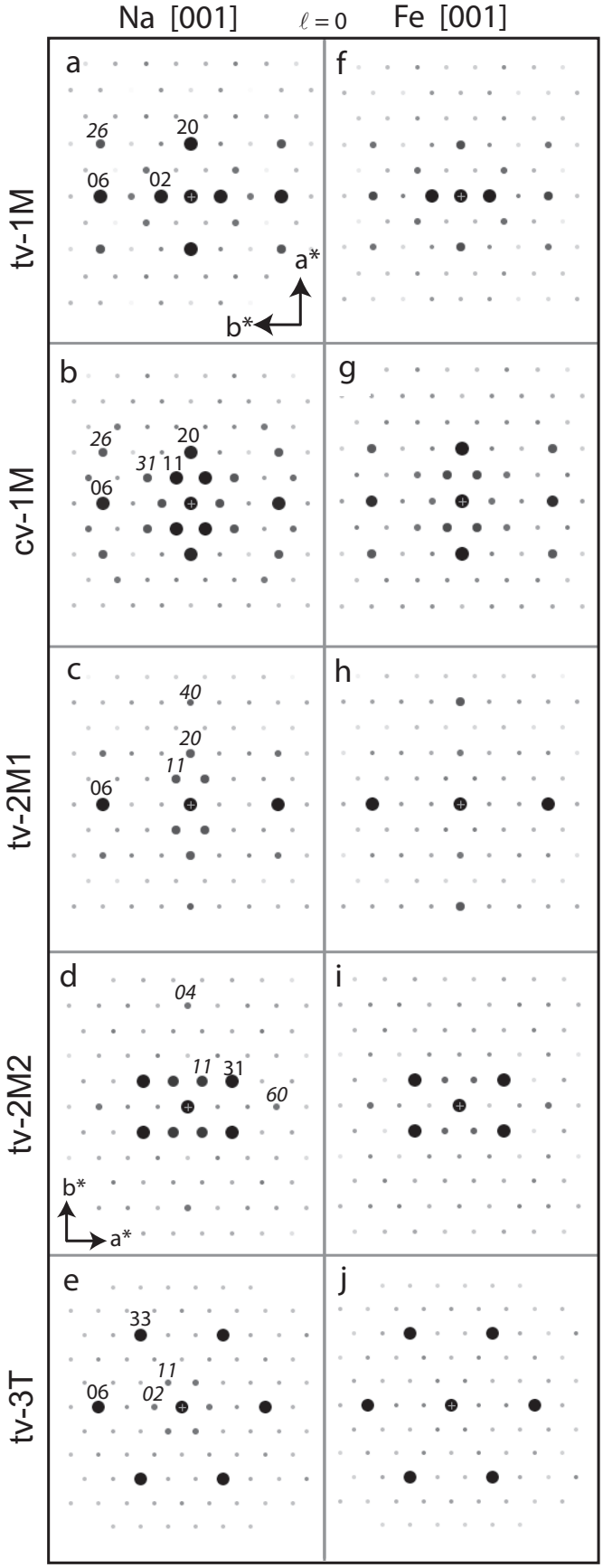

Figure

Click here to access/download;Figure;Figure 5.eps

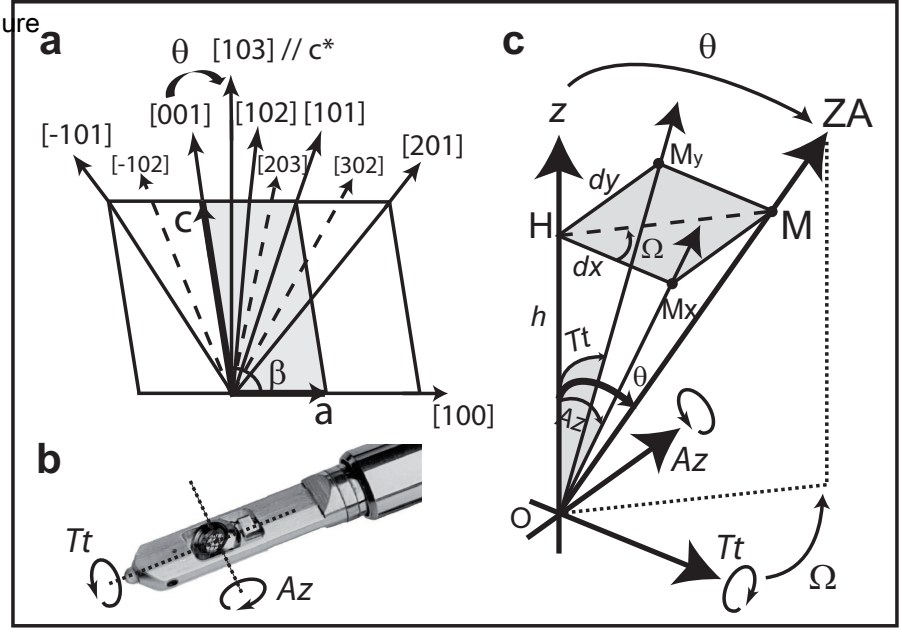

Figure

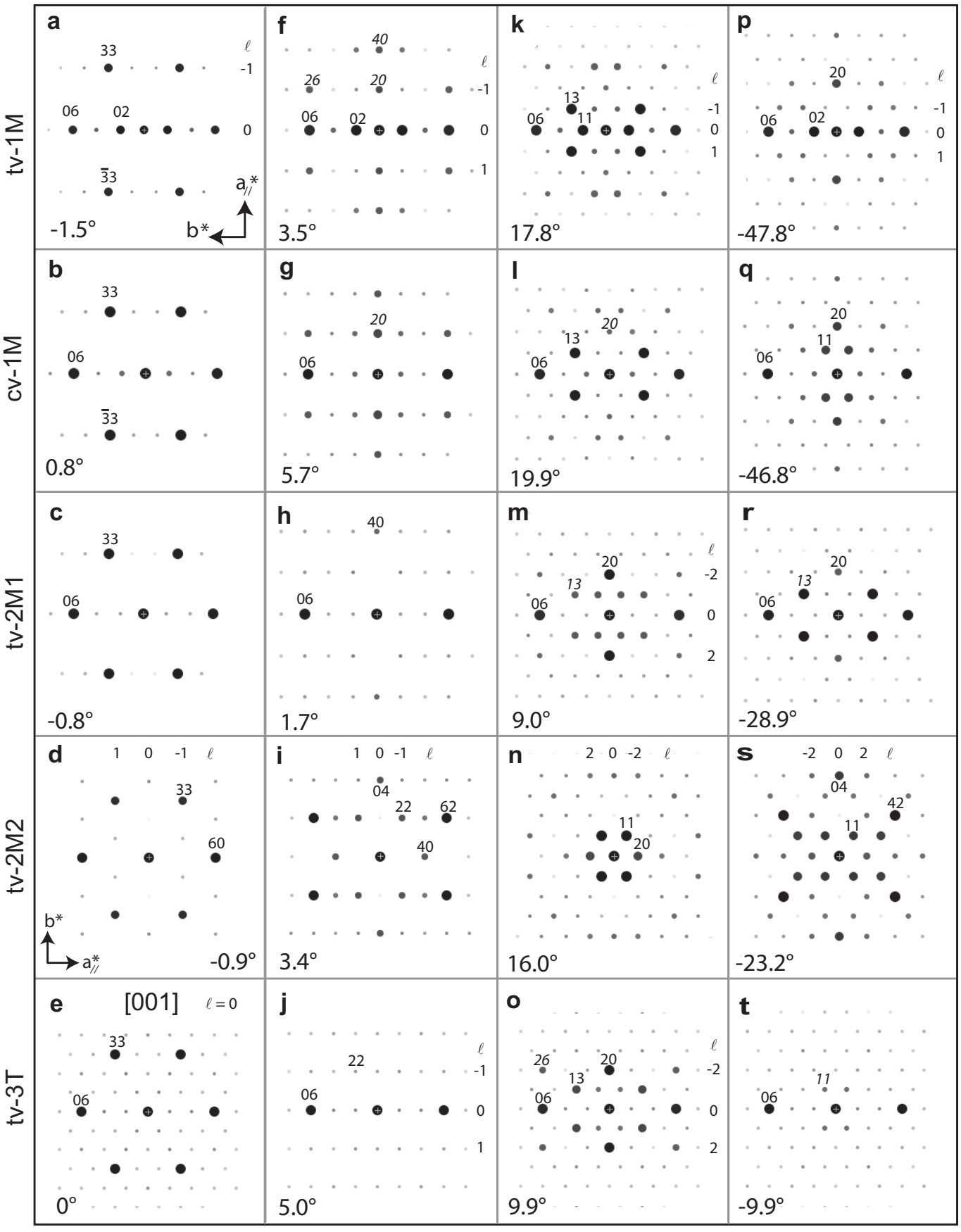

Figure

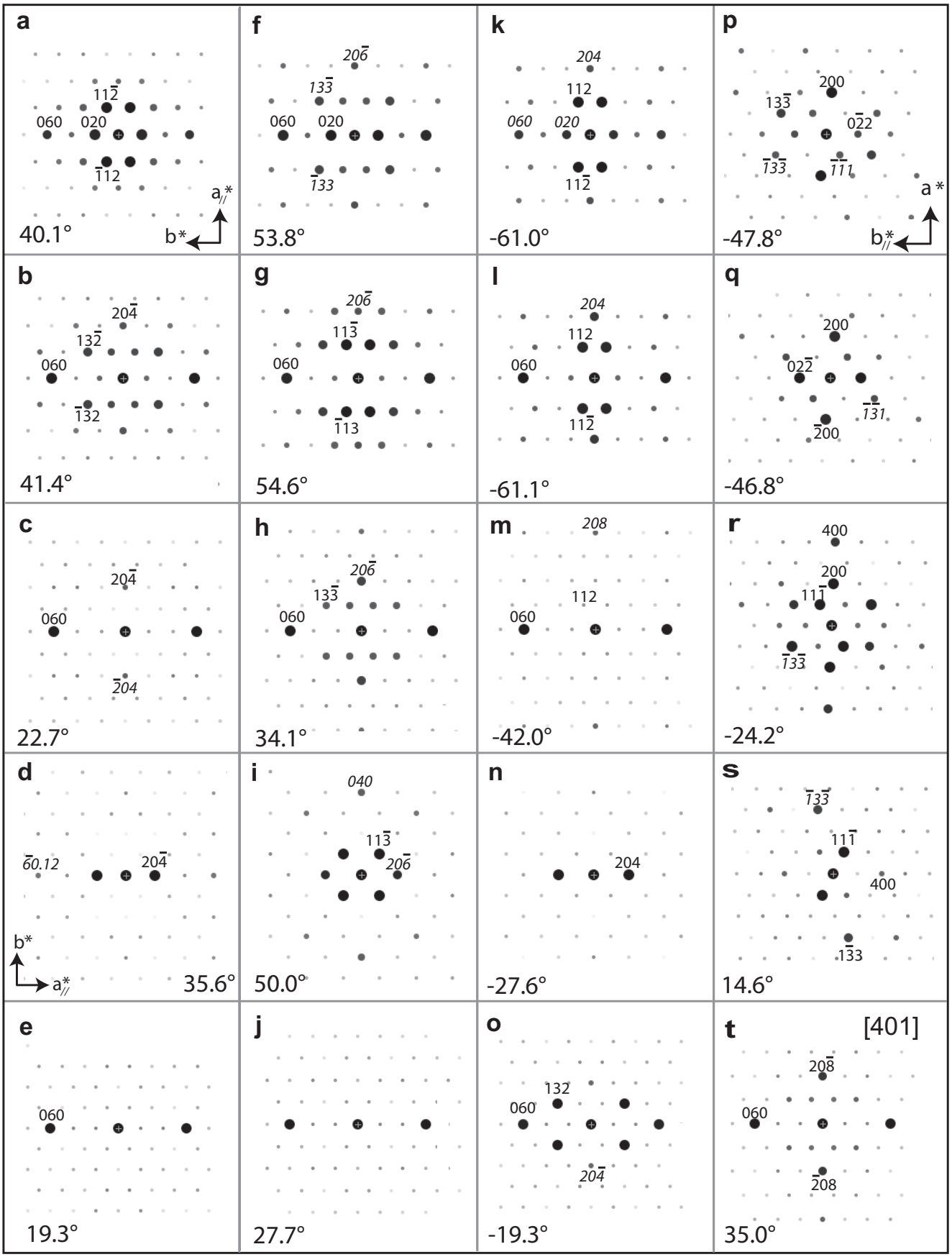

Figure

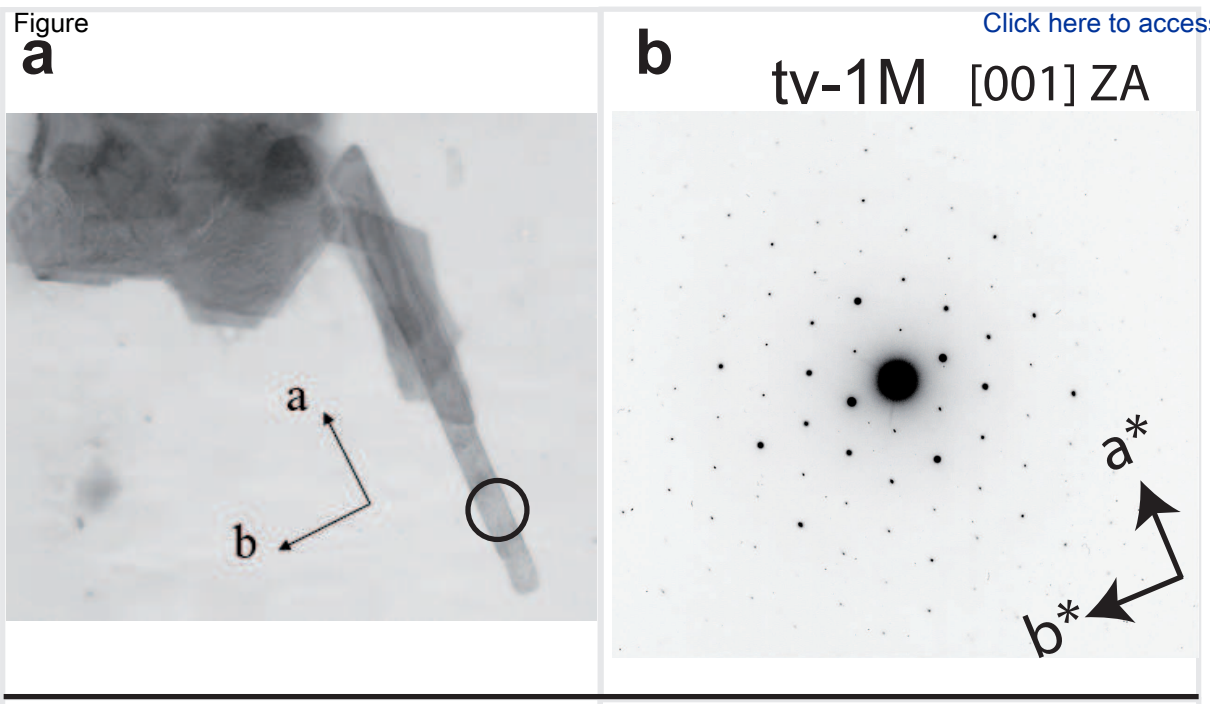

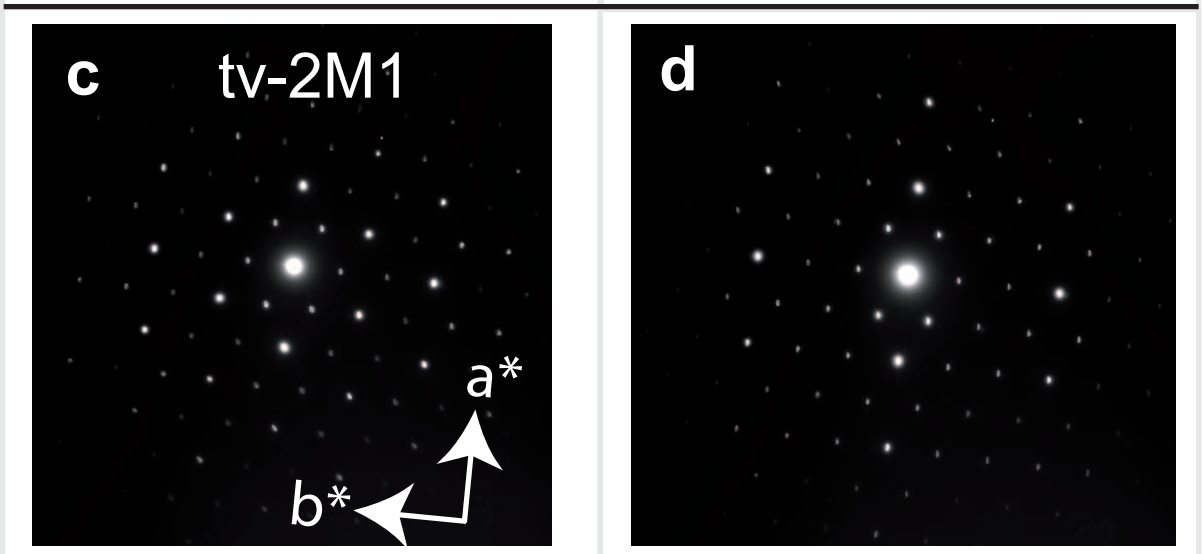

Tilt = -10.1°, Az = +6.4°

$|\theta|_{exp}$ = 11.9°

[101] ZA ; θ_{th} = -9.0°

Tilt = +1.8°, Az = -5.6°

$|\theta|_{exp}$ = 2.9°

[001] ZA ; θ_{th} = -5.8°

Gaillot et al. - Figure 8